IOP Publishing Nanotechnology
Nanotechnology 32 (2021) 205301 (10pp) https://doi.org/10.1088/1361-6528/abe4fc

Magnetically responsive polymer nanopillars with nickel cap

Zhiren Luo[1], Xu A Zhang[2] and Chih-Hao Chang[1]

[1] Walker Department of Mechanical Engineering, University of Texas at Austin, Austin, TX 78712, United States of America
[2] Department of Mechanical and Aerospace Engineering, North Carolina State University, Raleigh, NC 27695, United States of America

E-mail: chichang@utexas.edu

Received 24 November 2020, revised 28 January 2021
Accepted for publication 10 February 2021
Published 24 February 2021

Abstract

Embedding magnetic particles within polymer matrix is a common and facile method to fabricate magnetically responsive micro-/nanoscale pillars. However, the balance between mechanical compliance and magnetic susceptibility cannot be decoupled and the particles are limited by the pillar feature size, which can limit the actuation performance. Here we demonstrate a new type of magnetically responsive nanostructure consisting of a polydimethylsiloxane (PDMS) nanopillar array with deposited nickel caps, that has successfully achieved such decoupling with multiple cap-geometry designs for a better actuation control. The actuation result of nanopillars with 540 nm period and 1.3 μm height has been analyzed using image processing, leading to a maximum displacement of 180 nm with a ratio of 13.9% with respect to the pillar height. Magnetic and mechanical models based on magnetic force and torque have been developed and used to mitigate the weakening effect of the actuation by the residual magnetic layer. This structure demonstrates a feasible strategy for magnetic actuation at the sub-micrometer scale with freedom to design magnetic cap and polymeric pillar separately. This structure can also be utilized in multiple applications such as tunable optical elements, dynamic droplet manipulation, and responsive particle manipulation.

Supplementary material for this article is available online

Keywords: nanopillar, responsive material, nanofabrication, magnetic structures

(Some figures may appear in colour only in the online journal)

Introduction

Magnetically responsive structures have attracted research attention due to their advantages such as low energy consumption, non-contact manipulation, and quick response time [1]. These structures can be in liquid state which are formed by ferrofluid that are quasi-stable [2, 3], or can be solid state such as thin film in macroscale [4]. As for more stable and smaller magnetically responsive structures, solid micro-/nanoscale pillars have been developed for many potential applications in microfluidics [5–7], tunable wetting [8–10], dynamic optics [3, 11], and cell manipulation [12, 13].

Several methods have been widely used to fabricate these responsive pillars. One common method to implement such magnetic responsive structure is to embed magnetic particles into compliant polymeric matrices [11–15]. In this approach a mold pattern with hole arrays is fabricated using lithographic techniques, which is filled with magnetic particles and pre-polymer. A variety of materials can be utilized as magnetic particles such as iron oxide [5], carbonyl iron [8], cobalt [9], NdFeB [14], and chromium dioxide [16], and the particle shapes can be spherical-like [5] or rod [12]. In some cases, the magnetic particles can be guided by external magnetic field to form heterogeneous concentration [17] or different directional self-assembly chains [18]. After curing and demolding using a peel-off process, polymeric pillars embedded particles can be fabricated. Other methods use dry or wet etching to remove the mold from replica pillars, resulting in high-aspect-ratio pillars

[5, 19]. Mold-free methods have also been implemented where the mixture of magnetic particles and polymer are cured in a strong magnetic field, leading to non-periodic micropillars [20, 21].

Where there has been exciting progress in magnetically responsive micropillars (feature size $>10\,\mu$m) [20–22], pillars with smaller feature sizes in submicro-/nanoscale have rarely been studied. As feature sizes become smaller, it becomes more likely to enable nanopillars to manipulate smaller length scale objects such as particulates, cells, and visible light. In addition, smaller structure behaves more like a continuous material, which is also important for the control of the actuation. However, there are still significant challenges to fabricate and actuate such submicro-/nanopillars. This can be attributed to the decrease of magnetic force at smaller length scale during the actuation, leading to the requirement of high-aspect-ratio pillars dominated by magnetic torque [19]. However, these tall pillars tend to collapse easily and make fabrication even more difficult [23]. The second challenge can be the size limitations of magnetic particles that are embedded in the polymer matrix. Nanoparticles (∼7 nm) can easily be applied into mold and facilitate the embedding process, but they are superparamagnetic [24, 25] with low saturation magnetization compared with microparticles [20, 22]. In particular, another essential challenge is the balance between the magnetic susceptibility and mechanical compliance, which are both influenced by the concentration of the magnetic particles [25]. While higher particle concentration increases magnetization, which is favorable for actuation, it also decreases pillar compliance and hinders actuation. Lower particle concentration improves mechanical compliance and facilitates the fabrication, but results in low magnetization. As a potential solution, magnetic materials such as nickel can be electrodeposited as rigid metal pillars directly into the mold, but this still reduces the mechanical compliance [10, 26]. Therefore, a fabrication method where the magnetic and mechanical properties can be independently designed needs to be developed to overcome such challenges for a better control of the pillar actuation.

In this work, a new magnetically responsive nanostructure based on polydimethylsiloxane (PDMS) nanopillar array with nickel cap and sidewall is demonstrated. The proposed approach can decouple the mechanical compliance and magnetic susceptibility by depositing ferromagnetic materials on the surfaces of soft pillars. The PDMS pillars is fabricated using soft lithography and can be trimmed using dry etching to achieve higher aspect ratio and mechanical compliance. The thickness of nickel cap can be increased readily by controlling the deposition time, leading to higher magnetization. Using this approach, pillars with height of 1.3 μm, diameter of 410 nm, and period of 540 nm have been fabricated and tested. Analytical models based on magnetic force, torque, and mechanical beam bending have been developed to describe the behaviors of the fabricated structures. It demonstrates that the aspect ratio is a critical factor for the actuation. The components of magnetic force and torque are characterized separately to analyze actuation modes. It can be observed that magnetic torque dominates at sub-micrometer scale. The actuation of the fabricated structures was implemented using permanent magnet and tracked using image analysis algorithms to characterize the movement of pillars over time. The magnetic shielding effect induced by the residual layer has been characterized and mitigated during the test. Finally, the displacements up to 180 nm with the ratio of 13.9% with respect to the pillar height can be achieved, which is consistent with analytical model.

This structure demonstrates a facile and feasible strategy for magnetic actuation of pillars with sub-micrometer scale. Existing tunable structures are mostly based on embedding magnetic particle, which has limited size and magnetization. This work circumvents this challenge by depositing the magnetic material on the pillar, which results in more continuous magnetic film with higher magnetic saturation. This allows the fabricated magnetic pillars in this work to demonstrate promising actuation with low-aspect-ratio pillars to mitigate structure collapse and reduce fabrication difficulty. In addition, the cap and pillar geometries can be tuned separately to achieve high magnetic susceptibility and the low mechanical compliance simultaneously, offering more design freedom. This structure can find various potential applications, such as dry adhesion, tunable optical elements, and cell manipulation

Experimental approach

The fabrication process for the proposed responsive PDMS pillars with nickel caps is illustrated in figure 1. First, antireflection coating (ARC) with 90 nm thickness and photoresist SU-8 with 1.3–2.7 μm thickness are spincoated on silicon substrates. Then the photoresist is exposed by two orthogonally exposures using Lloyd's mirror interference lithography [27–29] with 325 nm laser, resulting in two-dimensional (2D) periodic holes array, as shown in figure 1(a). In this work structures with periods of 540 nm and 2 μm were fabricated. The photoresist mold is then treated by oxygen plasma and trichloro(octyl)silane to decrease surface energy. PDMS with 1:10 mixing ratio is applied into the photoresist mold, cured, and demolded using soft lithography, resulting in a pillar array, as shown in figures 1(b) and (c).

In order to investigate the influence of magnetic force and torque in the actuation mechanism, two types of structures were fabricated separately after the soft lithography process. The Type I pillars are designed to be actuated by magnetic force. In this case, the PDMS pillar array can be trimmed to form narrow pillar base using O_2 and SF_6 reactive ion etching, leading to a higher aspect ratio, as shown in figure 1(d). Then nickel is deposited onto the PDMS pillars using electron-beam evaporation at normal incidence, resulting in the nickel-capped PDMS pillar array, as shown in figure 1(e). Note the Type I pillars are relatively isolated with low duty cycle, which is defined as the ratio of the pillar diameter to the period, resulting in significant residual layer on the substrate. When the external magnetic field is applied, the residual layer forms a large horizontal induced field inside and redirect the external magnetic field around it due to the high magnetic permeability and strong shape anisotropy. Similar to the magnetic shielding effects, the residual layer will partially block the induced field in the nickel caps, which

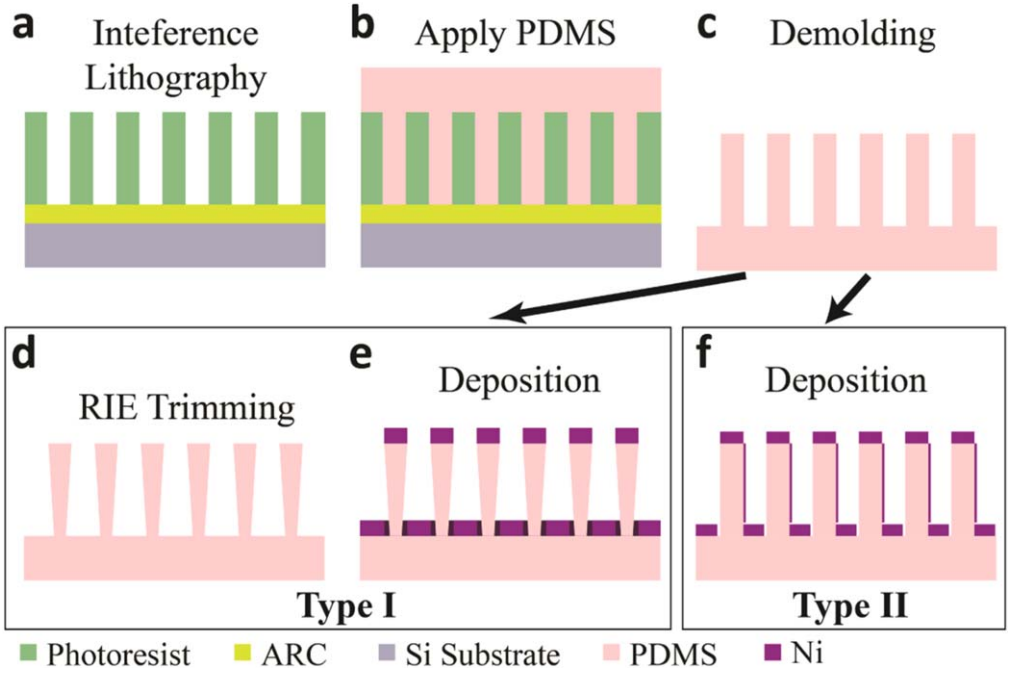

Figure 1. Fabrication processes of nickel-capped PDMS pillars. (a) The two-dimensional pattern is generated in photoresist using interference lithography. (b) PDMS is applied into the photoresist mold. (c) PDMS pillars is demolded. (d) The root of Type I pillar is trimmed using RIE. (e) The nickel is deposited onto the Type I pillars. (f) The nickel is deposited with a small tilted angle onto the Type II pillars.

will cause 'weakening effect' for actuation. The Type II pillars are designed to have both magnetic force and torque as actuation mechanisms, the latter of which can be enabled by having nickel film on the sidewalls. During the deposition, the pillar array is tilted at a small angle, resulting in thin nickel coating on the sidewall, as shown in figure 1(f). For these samples the PDMS pillars were deposited with nickel directly after soft lithography without trimming to maintain relatively high duty cycle. This leads to a more porous-like residual layer and a less weakening effect compared with the Type I pillars.

The scanning electronic microscope (SEM) images of nickel-capped PDMS pillars are depicted in figure 2. The Type I pillars have 2.7 μm pillar height, 600 nm top diameter, and 2 μm period, as shown in figure 2(a). The pillars are trimmed to have 310 nm bottom diameter, resulting in an aspect ratio of 8.7. The deposited nickel cap is 300 nm thick. Type II pillars have 1.3 μm pillar height, 410 nm diameter, and 540 nm period, as shown in figures 2(b) and (c). The nickel cap is 200 nm thick and the nickel sidewall is 11 nm thick, 280 nm wide, and around 1.3 μm high, as shown in figure 2(c). The nickel sidewall is thin and slightly porous instead of a continuous shell, which will not limit the mechanical compliance.

Modeling of structures

To characterize and predict the behaviors of these fabricated structures, analytical models based on magnetism and mechanics have been developed for both pillar types. For Type I pillars, a horizontal magnetic force $\boldsymbol{F}$ will form at the center of the nickel cap when a non-uniform horizontal external magnetic field $\boldsymbol{B}$ is applied. This force can be described as $\boldsymbol{F} = V\nabla(\boldsymbol{MB})$, where $\boldsymbol{M}$ is the magnetization of nickel cap and assumed to be homogeneous, $V = \pi\frac{D_2^2}{4}L_2$ is the volume of the nickel cap, L_2 is the nickel cap thickness, and D_2 is the top diameter of the pillar. To simplify the case, only the force component in x direction is considered, given by $F = F_x = VM_x\left(\frac{\partial B_x}{\partial x} + \frac{\partial B_z}{\partial x}\right)$. The field gradient $\frac{\partial B_x}{\partial x} + \frac{\partial B_z}{\partial x}$ is written as ∇B_x for convenience. More details regarding the derivation of magnetic force are discussed in supplementary section A (available online at stacks.iop.org/NANO/32/205301/mmedia). The horizontal magnetic force can be derived to be:

$$F = \pi\frac{D_2^2}{4}L_2M_x\nabla B_x. \quad (1)$$

To determine material properties, 2D finite element analyses (FEAs) models using the open-source software FEMM [30] were constructed to simulate the magnetic field, field gradient, and magnetization profiles. The external magnetic field is generated by a permanent magnet and can be simulated by the FEA model, as described in supplementary section A. The model indicates that at a distance of 3 mm away from the magnetic surface the magnetic field is $B \approx B_x = 0.2$ T, and B_z is nearly zero. The field gradient can also be calculated based on the field distribution, resulting in $\nabla B_x = 62\ \mathrm{T\ m^{-1}}$. The magnetization of the nickel caps and the residual layer are also simulated using FEA. Since it is difficult to describe the residual layer using 2D simulation, two geometries are simulated to determine the upper and lower range of the magnetic shielding effect for the residual layer. The first is the uniform residual layer without any holes, as shown in

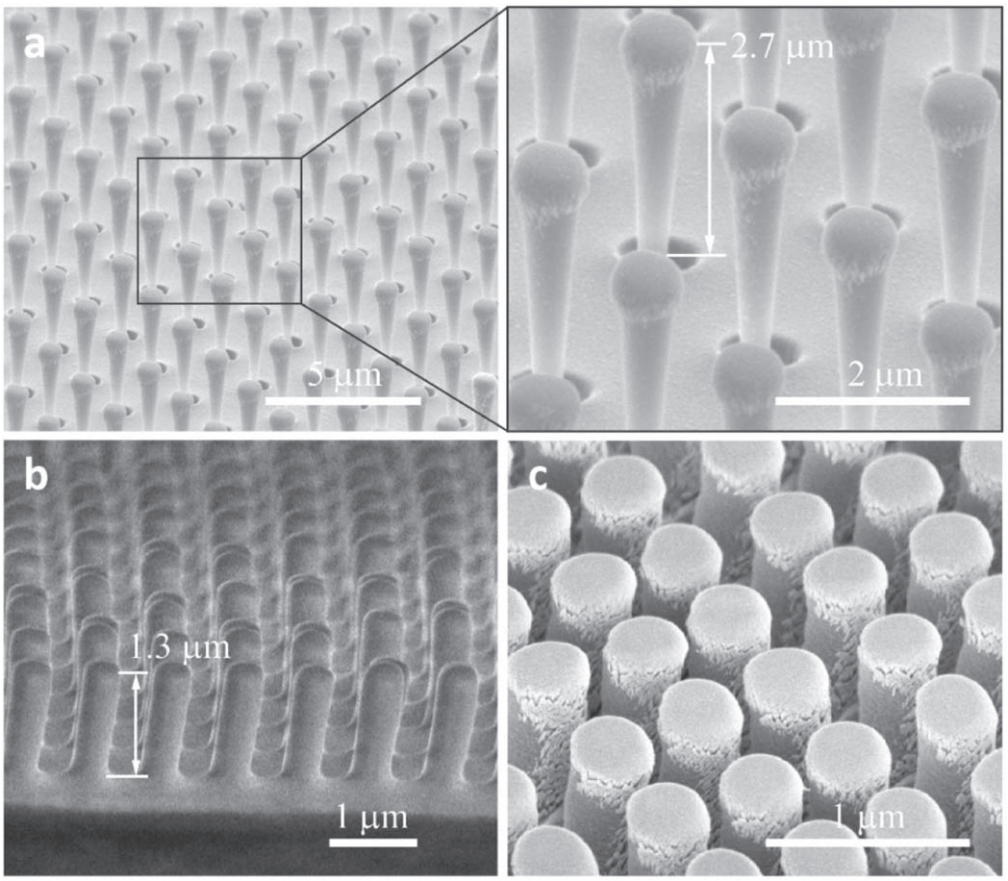

Figure 2. SEM images of nickel-capped PDMS pillar array. (a) The type I array with period of 2 μm. (b) The type II array before nickel deposition. (c) The type II array after nickel deposition.

figure 3(a), which would have more shielding effect than the real case. The second is the discrete residual layer with infinite depth in y direction (as shown in figure S3(a)), which will have less shielding effect than the real case, as discussed in supplementary section B. The induced magnetic fields B_{in} across the Type I nickel caps are extracted along the horizontal central line (red dashed line) at the center of the nickel caps and plotted in figure 3(b). Then the average of induced fields is calculated over the central line for cases of uniform and discrete residual layers, which are 0.51 T and 0.48 T, respectively. This indicates the difference between upper and lower range is small and the real case will be approximated by the average value $B_{\text{in}} = 0.5$ T. In addition, the nickel caps without residual layer are also simulated as a reference, as discussed in supplementary section B. The induced field without residual layer is around 0.56 T, which is 12% larger than the B_{in} of Type I pillars, demonstrating the magnetic shielding effect. The magnetization M can be expressed by the induced magnetic field B_{in}, that is $M_x = \frac{B_{\text{in}} - B}{\mu_0(1 - N_x)}$, where the $\mu_0 = 1.257 \times 10^{-6}$ H m^{-1} is the permeability of free space, the $N_x = 0.24$ is the demagnetizing factor of the nickel cap in horizontal direction [31]. As a result, the magnetization of Type I nickel cap is $M_x = 3.12 \times 10^5$ A m^{-1}.

In the mechanical model, the PDMS component of Type I pillar has taper geometry with the diameter decreasing gradually from top to bottom along the z direction, as shown in figure 3(c). The diameters on the bottom and top of the PDMS pillar are expressed as D_1 and D_2, respectively. The deflection of pillar with the gradually narrowed diameter can be derived from the Euler–Bernoulli equation. The derivation of the analytical model is discussed with more details in supplementary section C. The results indicate that the deflection δ_F and the bending angle θ_F can be given by:

$$\delta_F = \frac{64F}{3E\pi D_2} \cdot \left(\frac{L}{D_1}\right)^3 \cdot \left[1 + \frac{L_2}{4L}\left(\frac{D_1}{D_2} + 2\right)\right], \tag{2}$$

$$\theta_F = \frac{32FL_2L}{E\pi D_2^2 D_1^3} \cdot \left[\frac{L(D_1 + 2D_2)}{3L_2} + \frac{D_1^2 + D_2^2 + D_1D_2}{3D_2}\right], \tag{3}$$

where L is the height of PDMS pillar and $E = 600$ kPa is the Young's Modulus of PDMS. In addition, the nickel cap is regarded as rigid cylinder, leading to another component of displacement: $\theta_F L_2$. Therefore, the total displacement is:

$$\delta_{\text{I}} = \delta_F + \theta_F L_2. \tag{4}$$

The magnetic force can be substituted into the mechanical model by taking equations (1)–(3) into (4). In addition, the second order term $\frac{L_2^2}{L^2}$ can be ignored since L_2 is much smaller than L. Therefore, the displacement can be simplified as:

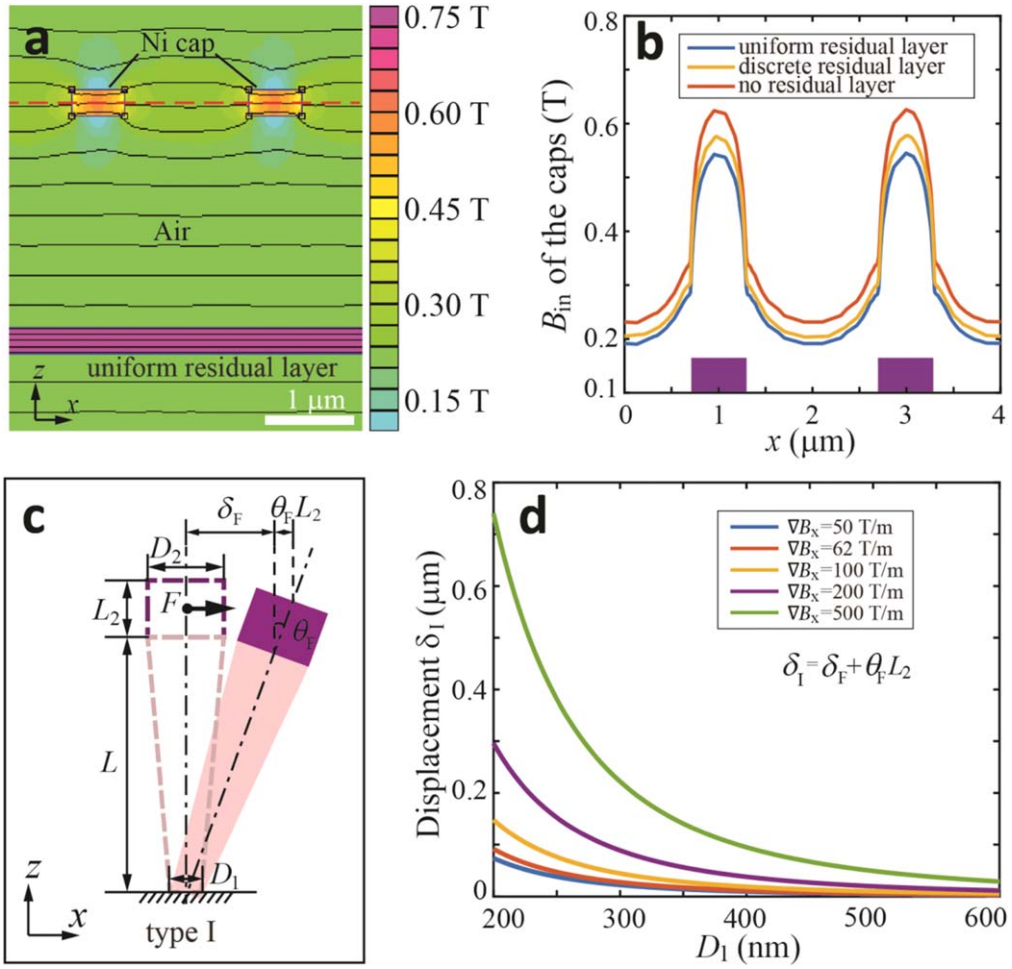

Figure 3. The analytical model of Type I pillars. (a) The magnetic flux density contour for nickel caps and the uniform residual layer. (b) The induced magnetic field of nickel caps. (c) The schematic of pillar dimension and the bending behavior. (d) The analytical displacements.

$$\delta_I = \frac{16 M_x D_2 L_2}{3E} \nabla B_x \left(\frac{L}{D_1}\right)^3 \left(1 + \frac{3}{4} \cdot \frac{D_1 + 2D_2}{D_2} \cdot \frac{L_2}{L}\right). \tag{5}$$

This model indicates that the displacement δ_I depends on material properties such as E, M_x, and ∇B_x, and ratios of geometry parameters such as $\frac{L}{D_1}$, $\frac{L_2}{L}$, and $\frac{D_1}{D_2}$. In particular, the aspect ratio of the pillar $\frac{L}{D_1}$ is critical since the δ_I is proportional to $\left(\frac{L}{D_1}\right)^3$. As described in the fabrication process, the bottom of pillar is trimmed using a plasma etching process to reduce D_1, leading to a higher aspect ratio $\frac{L}{D_1}$ and a larger displacement δ_I.

The displacement δ_I over bottom diameter D_1 with different field gradient have been plotted in figure 3(d). Here the parameters are $L = 2.7\ \mu$m, $D_2 = 600$ nm, $L_2 = 300$ nm based on the fabricated pillar parameters. It can be observed that as D_1 decreases, the δ_I will increase significantly. Large field gradient can also help to increase the displacement due to the linear proportional relationship. For the fabricated samples with bottom diameter $D_1 = 300$ nm and actuation gradient $\nabla B_x = 62$ T m^{-1}, the displacement δ_I is only around 27 nm. This limitation of the magnetic force actuation can be attributed to the relatively low aspect ratio of the fabricated Type I structures, and the low magnetic field gradients observed in macroscale permanent magnets. Larger displacement, such as $\delta_I = 214$ nm can be achieved by doubling the aspect ratio with $D_1 = 150$ nm and $\nabla B_x = 62$ T m^{-1}, and $\delta_I = 220$ nm can be achieved by a quintuple field gradient with $\nabla B_x = 500$ T m^{-1} and $D_1 = 300$ nm.

Another limitation of the magnetic force actuation for Type I pillars is that the residual layer weakens the magnetization due to the comparatively small duty cycle and the large exposed area on the base during the nickel deposition. To improve the actuation, two changes have been updated for the design of Type II pillars: nickel sidewall and a larger duty cycle. Type II pillars were designed so that the magnetic torque from nickel sidewall can also function as actuation mechanism, in additional to the magnetic force from the nickel cap seen in Type I pillars. The sidewall nickel film has a strong shape anisotropy along the z direction that can enable vertical magnetization, which initially might not be the direction of external magnetic field. As a result, a magnetic torque $\boldsymbol{\tau}$ will form due to the relative angle of the magnetization with respect of the external field, which is given by: $\boldsymbol{\tau} = V\boldsymbol{M}_{\text{wall}} \times \boldsymbol{B}$, where $V = wtL$ is the volume, w and t are the width and thickness of the sidewall, respectively,

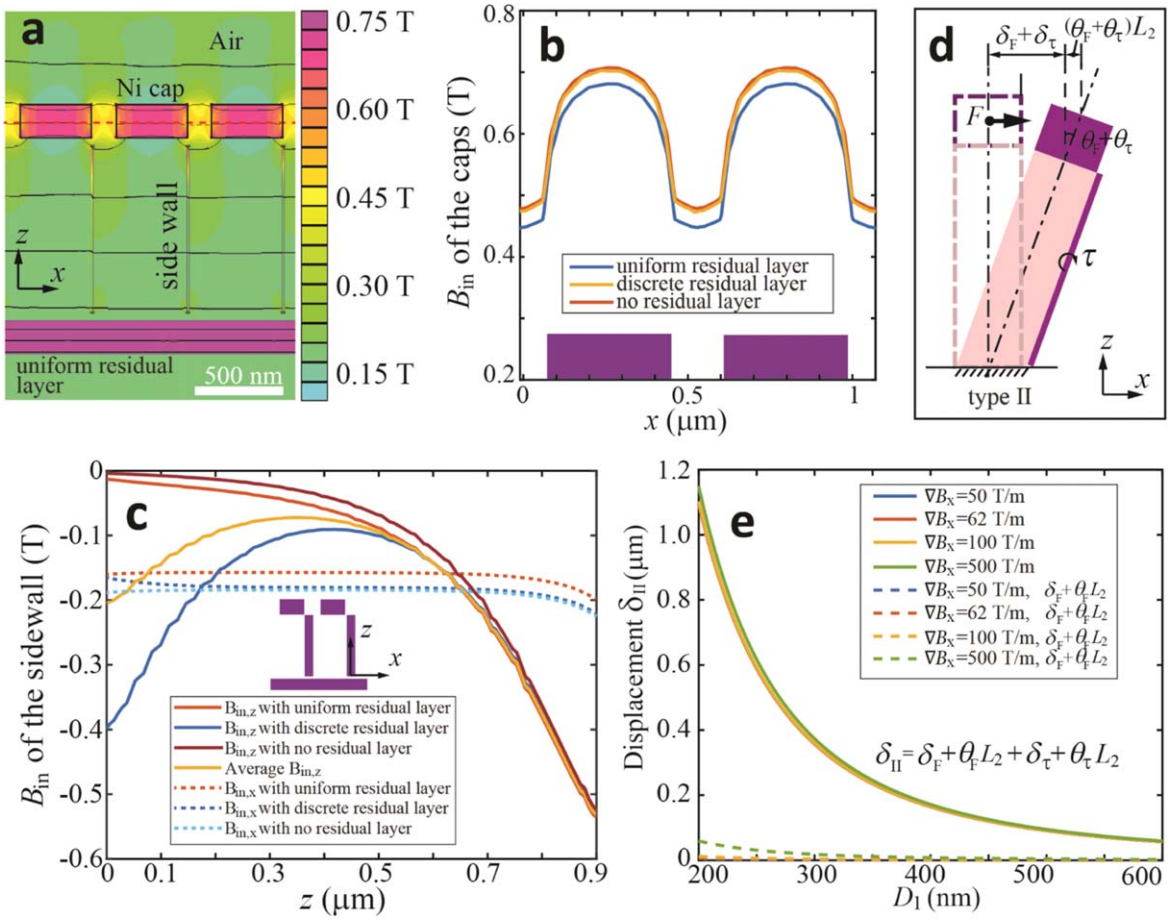

Figure 4. The analytical model of Type II pillars. (a) The magnetic flux density contour for nickel caps and the uniform residual layer. (b) The induced magnetic field of nickel caps. (c) The induced magnetic field of sidewalls. (d) The schematic of pillar dimension and the bending behavior. (e) The analytical displacements.

and $\boldsymbol{M}_{\text{wall}}$ is the magnetization of the sidewall. Given the shape anisotropy, $\boldsymbol{M}_{\text{wall}}$ is along z direction and $M_{\text{wall},x} = M_{\text{wall},y} = 0$. The external field component B_z is nearly zero but enough to induce the magnetization for the sidewall due to the shape anisotropy. The external field is set as $B_z = B_y = 0$ while $B_x = 0.2$ T. The length of the sidewall is assumed to be the same as the height of PDMS pillar L. As a result, the torque can be described as:

$$\tau_y = wtLM_{\text{wall},z}B_x. \tag{6}$$

Note the magnetic torque about the y axis (pointing into the plane) will also induce pillar bending towards the positive x direction, which is the same actuation direction caused by the magnetic force described previously. Similar to Type I, the magnetic force from the nickel cap is given by equation (1).

The magnetic response of nickel caps, sidewalls, and the residual layer for Type II pillars is also simulated using FEA. The contour of induced magnetic field distribution is shown in figure 4(a). It should be noted that the Type II caps are closer to each other and the Type II residual layer has less unit area. This can be described by the duty cycle. The Type I duty cycle is 0.3 while the Type II duty cycle is 0.76, indicating that a larger duty cycle leads to a less magnetic shielding effect from the residual layer. The curves of induced magnetic field across the nickel caps are plotted in figure 4(b). It can be observed that the Type II pillars have larger magnetization inside the caps than the Type I pillars. The B_{in} with uniform and discrete residual layers are 0.66 T and 0.63 T, respectively. The real case will then be approximated by the average $B_{\text{in}} = 0.65$ T. The B_{in} without residual layer is around 3% larger than the B_{in} of Type II pillars, verifying the less shielding effect. The magnetization of Type II nickel cap is $M_x = 4.66 \times 10^5$ A m^{-1}, which is close to the saturated magnetization of bulk nickel (5.1×10^5 A m^{-1}) [32, 33]. This is a 49.4% improvement compared with Type I pillars.

The induced magnetic field components inside the sidewall over x and z directions, which are $B_{\text{in},x}$ and $B_{\text{in},z}$, respectively, were examined with uniform and discrete residual layers, as plotted in figure 4(c). The component $B_{\text{in},x}$ is around 0.2 T, which is close to B and indicates that the $M_{\text{wall},x}$ is nearly zero, as expected. The component $B_{\text{in},z}$ in the sidewall with the uniform and discrete residual layers have a difference close to the residual layer when $z < 400$ nm. The $B_{\text{in},z}$ with uniform residual layer is nearly zero in this region, while $B_{\text{in},z}$ with discrete residual layer has a negative value, indicating the influence from the discrete residual layer. As the reference, the $B_{\text{in},z}$ without residual layer is also nearly zero in this region, verifying the difference and geometric influence above. The average $B_{\text{in},z}$ of sidewall with

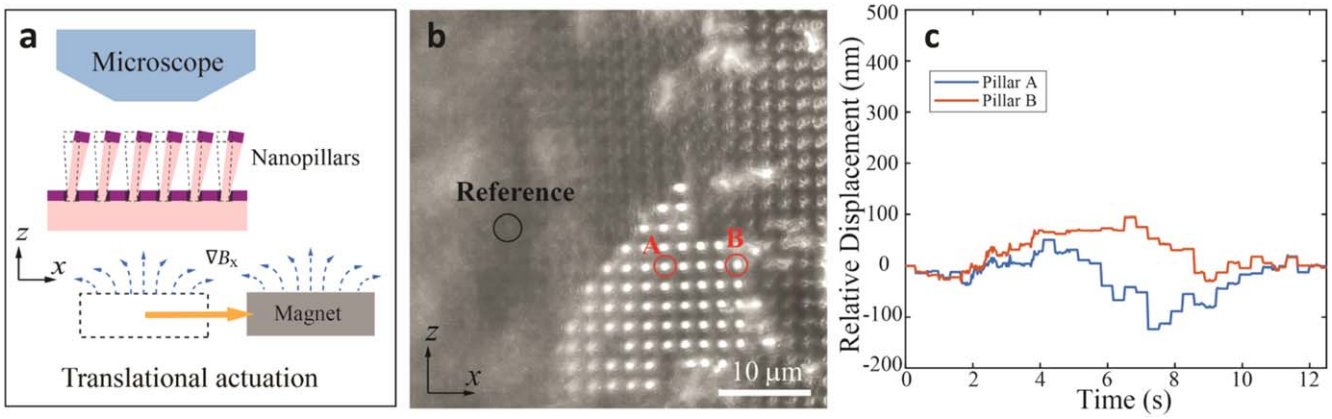

Figure 5. The experimental results of Type I pillars. (a) The schematic of actuation setup. (b) The top-view microscope image. (c) The relative displacements of nanopillars.

uniform and discrete residual layers are also shown in figure 4(c). The magnetization of the sidewall can be calculated using $M_{\text{wall},z} = \frac{B_{\text{in},z} - B_z}{\mu_0(1-N_z)} = 1.40 \times 10^5\ \text{A m}^{-1}$. Here, the B_z is nearly zero and the demagnetizing factor in z direction N_z is also nearly zero due to the shape anisotropy.

The deflection mechanism for Type II pillars is different from Type I, and the torque component needs to be considered. The schematic of the mechanical model is illustrated in figure 4(d). The deflection of Type II PDMS pillar under the magnetic torque can also be derived from the Euler–Bernoulli equation, as detailed in supplementary section C. The deflection δ_τ and the bending angle θ_τ can be derived to be functions of the magnetic torque, as given by

$$\delta_\tau = \frac{32\tau}{3E\pi} \cdot \left(\frac{L}{D_1}\right)^2 \cdot \frac{D_1 + 2D_2}{D_2^2 D_1}, \tag{7}$$

$$\theta_\tau = \frac{64\tau}{3E\pi} \cdot \left(\frac{L}{D_1}\right) \cdot \frac{D_1 + 2D_2}{D_1^2 D_2^2}. \tag{8}$$

The deflection under the magnetic force of Type II pillar can be described by the same way as shown in Type I pillar, as described by equations (2)–(4). The total displacement is

$$\delta_{\text{II}} = \delta_F + \delta_\tau + (\theta_F + \theta_\tau)L_2, \tag{9}$$

where the second term describes the rigid-body rotation of the pillar cap. Finally, equations (1)–(3) and (6)–(8) are taken into equation (9). In addition, the second order term $\frac{L_2^2}{2L^2}$ can be ignored here since L_2 is also much smaller than L for Type II nanopillar. Therefore, the final displacement can be simplified as:

$$\delta_{\text{II}} = \frac{64}{E\pi D_2}\left(\frac{L}{D_1}\right)^3\left[M_x \frac{\pi}{4} D_2^2 L_2 \nabla B_x \left(\frac{1}{3} + \frac{D_1 + 2D_2}{4D_2} \cdot \frac{L_2}{L}\right) + wtM_{\text{wall},z}B_x \frac{D_1 + 2D_2}{3D_2}\left(\frac{1}{2} + \frac{L_2}{L}\right)\right]. \tag{10}$$

The total displacement of Type II pillars δ_{II} as a function of the bottom diameter D_1 has been plotted in figure 4(e) with different field gradients ∇B_x. Here the parameters are $L = 1.3\ \mu\text{m}$, $D_2 = 400\ \text{nm}$, $L_2 = 200\ \text{nm}$, $t = 11\ \text{nm}$, $w = 280\ \text{nm}$ based on the dimensions of fabricated Type II pillars. Similar to Type I pillars, the displacement will increase significantly when D_1 is decreased. For similar magnetic actuation conditions where $D_1 = 410\ \text{nm}$ and $\nabla B_x = 62\ \text{T m}^{-1}$, δ_{II} is 154 nm, roughly as 6 times as the δ_{I} for Type I pillars. However, the increasing field gradient does not improve the displacement, indicating that the dominant actuation mechanism is not related to magnetic force. To examine the effects of the magnetic force *versus* torque, displacement components attributed to magnetic force, $\delta_F + \theta_F L_2$ are also plotted as dashed curves. It can be observed that the contribution is small, demonstrating that the component attributed to magnetic torque $\delta_\tau + \theta_\tau L_2$ is dominant term in δ_{II}. In addition, under same external magnetic field and field gradient, the Type II pillar can achieve larger displacement of 154 nm with low aspect ratio around 3.2 while the Type I pillars with high aspect ratio of 8.7 can only have analytical displacement of 27 nm. For Type II pillars, a higher aspect ratio of 6 with $D_1 = 216\ \text{nm}$ can enable a displacement of 800 nm based on the analytical model. In addition, doubling the thickness of 22 nm for the nickel sidewall can double the torque and leads to a displacement of 326 nm, since this is still thin sidewall and the mechanical compliance can be assumed not changed. This indicates that magnetic torque is more efficient actuation mechanism than magnetic force in sub-micrometer scale when using a permanent magnet.

Result and discussion

The actuation of the fabricated Type I and II pillars are examined by translating a permanent magnet under the pillars manually. First, the Type I nanopillars is actuated to translate in positive x direction, as illustrated in the schematic setup in figure 5(a). The nanopillars are initially located at 3 mm above and along the centerline of the magnet, where the external magnetic field is pointing up with around 0.2 T. In this case, the nanopillars stand vertically, as shown in dashed pillars and magnet in figure 5(a). The magnet is then translated toward the positive x direction, tilting the magnetic field

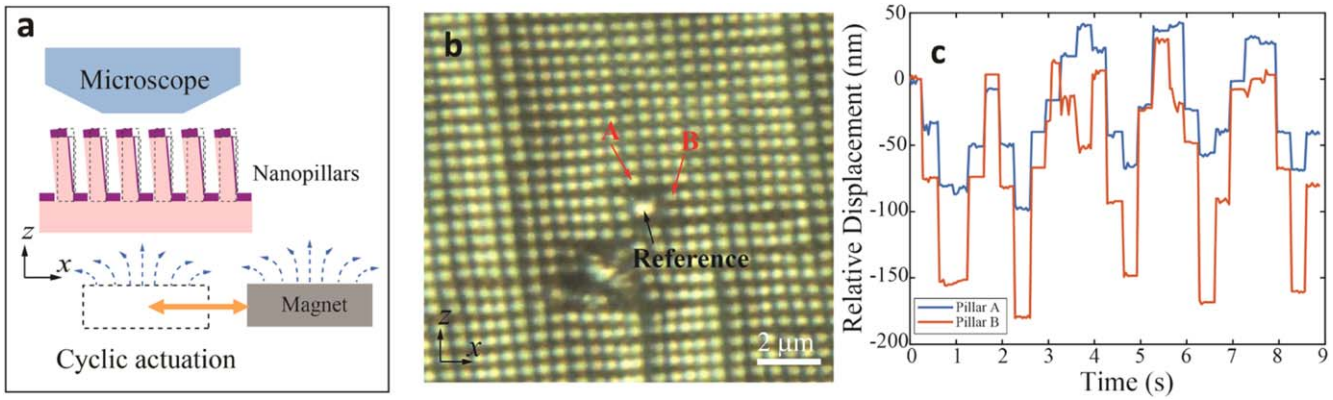

Figure 6. The experimental results of Type II pillars. (a) The schematic of actuation setup. (b) The top-view microscope image. (c) The relative displacements of nanopillars.

and inducing a displacement at the top of the nanopillars in the same direction. When the magnet moves to the position where its edge is under the nanopillars, the magnetic field gradient would achieve a peak around 62 $\mathrm{T\,m^{-1}}$ while the field is still around 0.2 T, as discussed in supplementary section A. In this case, the nanopillars is actuated to have maximum displacement. When the magnet translates farther, the field and field gradient both decrease, leading to a decrease of the actuated pillar displacement.

The displacement of Type I nanopillars is observed using top-view optical microscopy and recorded as supplementary movie 1. The extracted images during actuation are shown in figure 5(b). Three positions have been chosen to characterize the displacements including two pillars at A and B. A black circle denotes a hole in the residual layer where a pillar has broken off to serve as a reference to characterize the substrate movement. The relative displacements of pillar A and B with respect to the reference are analyzed and plotted in figure 5(c) using the custom-built code through software ImageJ and Matlab. This image analysis method is based on tracking the relative motion using a correlation kernel, and has been described with details in our previous work [19]. Pillar B can achieve a peak relative displacement of 95 nm, which matches the order of magnitude of the analytical model. However, pillar A has a negative peak relative displacement around −124 nm, which indicates that the actuation and movement of the base is even greater than pillar A. It is important to note that the peak displacement of the base is three-fold larger than the peak relative displacements of pillar A and B (as shown in figure S6). This large displacement can be due to the residual layer, which has a large magnetization and generates a strong magnetic force during the actuation. This can be verified by the simulation in figure 3(b). More details are also discussed in supplementary section D. In addition, the aspect ratio is still not high enough to generate large relative displacement.

Type II nanopillars are actuated in similar manner, as illustrated in the setup schematic in figure 6(a). The nanopillars are initially located along the center line and 3 mm above the permanent magnet, as shown by the dashed lines in the schematic. The magnet then translates toward positive x direction until the nanopillars are above the edge of the magnet and then moves back to initial position. Different from Type I pillars, the Type II pillars tilt along the field lines in the negative x direction. The duration of the actuation is around 9 s with 5 cycles. The actuation of Type II nanopillars is also observed using top-view microscope and recorded as supplementary movie 2 with the extracted images, as shown in figure 6(b). Three positions are also chosen here, including pillars A and B to examine actuation. The collapse of four pillars can be observed in the image, and is chosen as the reference to characterize the base movement. The relative displacements of pillar A and B with respect to the base are analyzed and plotted as blue and red solid curves in figure 6(c). There are 5 cycles in the relative displacement curves. Pillar B has peak displacement up to −180 nm during the actuation, which matches with the analytical model with around 17% error. Here, the minus means the pillar is tilted toward negative x direction to align with the field lines. Pillar A can achieve peaks as high as −99 nm, which is around 36% less than the analytical prediction. The peak of the base is around 70 nm in each cycle while there is a drift of about 100 nm toward the negative x direction during the entire actuation, as discussed in supplementary section D. The displacement of the base is attributed to the magnetization from the residual layer. However, this is less than one forth of the displacement for the Type I base, illustrating a decrease of weakening effect. The peaks of relative displacements of pillar A and B are 43% and 157% larger than the peak displacement of the base, respectively. This demonstrates that the magnetic torque enables the Type II pillars to achieve large deflections even though there is a weakening effect from the residual layer.

The movement of the pillar base due to the residual layer is critical in analyzing the actuation of the pillars. The residual layer is more porous and has lower magnetization in Type II pillars than Type I pillars, resulting in a much smaller displacement of the base. Therefore, the parameter duty cycle can be used to determine the topography and actuation of the residual layer. A larger duty cycle induces a lower weakening effect for actuation. Another critical factor is the magnetic torque in Type II nanopillars, which leads to a significant

improvement of the pillar deflection. Here, the actuation ratio can be defined as the ratio between the total displacement and pillar height to compare the bending deflection for two types of pillars. As a result, the actuation ratio of Type I nanopillar is about 3.3%, while the actuation ratio of Type II nanopillars is around 13.9%, demonstrating the actuation improvement.

In addition, Type II nanopillars can achieve such actuation ratio with a low aspect ratio of 3.2. In comparison, such actuation ratio (13.9%) would require a quite high aspect ratio for pillars which have coupled magnetic susceptibility and mechanical compliance. For example, it has been published in our previous work that the high-aspect-ratio ($\sim$11) nanopillars with iron oxide nanoparticles imbedded can achieve actuation ratio of 2.9% with respect to 7 μm pillar height [19]. This demonstrates the advantage of the decoupling and the magnetic torque in this work. It also indicates the feasibility to achieve displacement of around 150 nm with relatively low aspect ratio at sub-micrometer scale, which reduces the fabrication difficulty for Type II pillars.

Conclusion

The magnetic material and polymer have been decoupled in this work as a potential strategy of magnetic actuation. Two types of nanopillars have been designed and investigated with respect to cap geometry, duty cycle, and aspect ratio. Type I pillars has magnetic caps and are actuated by magnetic force. Type II pillars have magnetic caps and sidewalls and can be actuated by a combination of magnetic force and torque. It demonstrates that magnetic torque induced by cap sidewall and aspect ratio play critical roles in actuation, and duty cycle is important to reduce shielding effect from residual layers.

The strategy of this work removes the need for magnetic particle to decouple the magnetic and mechanical properties of the nanopillars. By controlling the magnetic film on top and side of pillars, the structures can be actuated to have displacement around 185 nm with a low aspect ratio, demonstrating a better actuation performance compared with particle imbedded pillars. Future work will focus on the design of nickel cap geometry, such as sidewall thickness and width, to further improve the actuation range. The pillar duty cycle can also be optimized as well to reduce the shielding effect. In addition, higher aspect ratio will be used to increase the magnetic torque and improve the deflection significantly. This work can find potential applications in various areas, such as tunable optical elements, cell manipulation, and nanofluidics.

Methods

Fabrication of PDMS pillars with Nickel caps

First, ARC (ARC i-con-7, Brewer Science) with 90 nm thickness is spincoated on silicon substrates and baked at 185 °C on hotplate for 1 min. Then the photoresist (SU-8 2005, Kayaku Advanced Materials) with 1.3–2.7 μm thicknesses is spincoated onto ARC and soft baked at 90 °C on hotplate for 1 min. After exposure using Lloyd's mirror interference lithography, the photoresist is post-exposure baked at 90 °C for 3 min on a hotplate, developed in PGMEA for 1 min, and rinsed with deionized water. The photoresist mold is then treated by oxygen plasma for 1 min in oxygen plasma cleaner and put in vacuum with trichloro (octyl)silane (Sigma-Aldrich) vapor for 6 h. The silane will be coated onto photoresist mold to decrease the surface energy. PDMS (Sylgard 184, Dow Corning) with 1:10 mixing ratio is applied into the photoresist mold, cured at 100 °C on hotplate for 1 h, and demolded be mechanical peeling. Nickel is deposited onto PDMS pillars using electron-beam evaporation.

Simulations and software

The analytical models are approached using custom-written code in Matlab. The numerical simulations are approached using open-source software FEMM and corresponding results are analyzed using Matlab. The microscope images are basically analyzed using open-source software ImageJ.

Material characterization

The SEM images are taken by FEI Quanta 3D FEG. The top-view microscope images are recorded using Leitz Wetzlar microscope with 1000× magnification. The magnet in this work is a cylindrical FeNdB permanent magnet (J&K magnetics) with diameter of 25.4 mm and length of 6.35 mm. The magnetic field around the magnet is simulated using FEMM and experimentally measured by Guassmeter Model GM-2 (Alphalab Inc.).

Acknowledgments

This work was performed at the NCSU Nanofabrication Facility (NNF), the Analytical Instrumentation Facility (AIF), and the members of the North Carolina Research Triangle Nanotechnology Network (RTNN), supported by the National Science Foundation as part of the National Nanotechnology Coordinated Infrastructure (NNCI). This work was also performed at NAnomanufacturing Systems CENTer (NASCENT), Texas Materials Institute (TMI), and Texas Nanofabrication Facility supported by NSF grant NNCI-2025227. This work was supported by the Defense Advanced Research Projects Agency (DARPA) under grant W911NF-15-1-0108 and partially supported by National Science Foundation (NSF) grant CMMI#1552424.

Data availability statement

All data that support the findings of this study are included within the article (and any supplementary files).

Author contributions

C-HC conceived of the idea and supervised the study. ZL performed the experiments, developed the models, and wrote the manuscript. XZ helped to develop the fabrication. All the authors contributed to the paper revision and approved the finalized manuscript.

Competing interests

The authors declare no competing financial interests.

ORCID iDs

Zhiren Luo https://orcid.org/0000-0001-6247-0196

References

[1] Zhang X, Sun L, Yu Y and Zhao Y 2019 Flexible ferrofluids: design and applications *Adv. Mater.* **31** 1903497
[2] He L, Wang M, Zhang Q, Lu Y and Yin Y 2013 Magnetic assembly and patterning of general nanoscale materials through nonmagnetic templates *Nano Lett.* **13** 264–71
[3] Luo Z, Evans B A and Chang C-H 2019 Magnetically actuated dynamic iridescence inspired by the neon tetra *ACS Nano* **13** 4657–66
[4] Kim Y, Yuk H, Zhao R, Chester S A and Zhao X 2018 Printing ferromagnetic domains for untethered fast-transforming soft materials *Nature* **558** 274–9
[5] Evans B A *et al* 2007 Magnetically actuated nanorod arrays as biomimetic cilia *Nano Lett.* **7** 1428–34
[6] Fahrni F, Prins M W J and van IJzendoorn L J 2009 Micro-fluidic actuation using magnetic artificial cilia *Lab Chip* **9** 3413–21
[7] Shields A R *et al* 2010 Biomimetic cilia arrays generate simultaneous pumping and mixing regimes *Proc. Natl Acad. Sci. USA* **107** 15670–5
[8] Drotlef D-M, Blümler P, Papadopoulos P and del Campo A 2014 Magnetically actuated micropatterns for switchable wettability *ACS Appl. Mater. Interfaces* **6** 8702–7
[9] Cao M *et al* 2014 Facile and large-scale fabrication of a cactus-inspired continuous fog collector *Adv. Funct. Mater.* **24** 3235–40
[10] Zhu Y, Antao D S, Xiao R and Wang E N 2014 Real-time manipulation with magnetically tunable structures *Adv. Mater.* **26** 6442–6
[11] Liu S, Long Y, Liu C, Chen Z and Song K 2017 Bioinspired adaptive microplate arrays for magnetically tuned optics *Adv. Opt. Mater.* **5** 1601043
[12] Sniadecki N J *et al* 2007 Magnetic microposts as an approach to apply forces to living cells *Proc. Natl Acad. Sci. USA* **104** 14553–8
[13] Khademolhosseini F and Chiao M 2013 Fabrication and patterning of magnetic polymer micropillar structures using a dry-nanoparticle embedding technique *J. Microelectromech. Syst.* **22** 131–9
[14] Drotlef D-M, Blümler P and Campo A. del 2013 Magnetically actuated patterns for bioinspired reversible adhesion (dry and wet) *Adv. Mater.* **26** 775–9
[15] Zhang S, Wang Y, Onck P R and den Toonder J M J 2019 Removal of microparticles by ciliated surfaces—an experimental study *Adv. Funct. Mater.* **29** 1806434
[16] Li M *et al* 2018 Flexible magnetic composites for light-controlled actuation and interfaces *Proc. Natl Acad. Sci.* **115** 8119–24
[17] Wang Z *et al* 2020 Hybrid magnetic micropillar arrays for programmable actuation *Adv. Mater.* **32** 2001879
[18] Jeon J *et al* 2020 Shape-programmed fabrication and actuation of magnetically active micropost arrays *ACS Appl. Mater. Interfaces* **12** 17113–20
[19] Luo Z, Zhang X A, Evans B A and Chang C-H 2020 Active periodic magnetic nanostructures with high aspect ratio and ultrahigh pillar density *ACS Appl. Mater. Interfaces* **12** 11135–43
[20] Huang Y *et al* 2017 A switchable cross-species liquid repellent surface *Adv. Mater.* **29** 1604641
[21] Lee S-H *et al* 2018 Tunable multimodal drop bouncing dynamics and anti-icing performance of a magnetically responsive hair array *ACS Nano* **12** 10693–702
[22] Peng Y *et al* 2015 Magnetically induced fog harvesting via flexible conical arrays *Adv. Funct. Mater.* **25** 5967–71
[23] Zhang Y, Lo C-W, Taylor J A and Yang S 2006 Replica molding of high-aspect-ratio polymeric nanopillar arrays with high fidelity *Langmuir* **22** 8595–601
[24] Jeong U, Teng X, Wang Y, Yang H and Xia Y 2007 Superparamagnetic colloids: controlled synthesis and niche applications *Adv. Mater.* **19** 33–60
[25] Evans B A *et al* 2012 A highly tunable silicone-based magnetic elastomer with nanoscale homogeneity *J. Magn. Magn. Mater.* **324** 501–7
[26] Grigoryev A, Tokarev I, Kornev K G, Luzinov I and Minko S 2012 Superomniphobic magnetic microtextures with remote wetting control *J. Am. Chem. Soc.* **134** 12916–9
[27] Isapour G and Lattuada M 2018 Bioinspired stimuli-responsive color-changing systems *Adv. Mater.* **30** 1707069
[28] Smith H I 2001 Low cost nanolithography with nanoaccuracy *Physica* E **11** 104–9
[29] Bagal A and Chang C-H 2013 Fabrication of subwavelength periodic nanostructures using liquid immersion Lloyd's mirror interference lithography *Opt. Lett.* **38** 2531–4
[30] Meeker D 2009 Finite Element Method Magnetics, Version 4.2 (http://www.femm.info)
[31] Osborn J A 1945 Demagnetizing factors of the general ellipsoid *Phys. Rev.* **67** 351–7
[32] Crangle J and Goodman G 1971 The magnetization of pure iron and nickel *Proc. R. Soc.* A **321** 477–91
[33] 1966 *Metals Handbook* vol 1 (Materials Park, Geauga County, Ohio: American Society for Metals)